Tailoring Staircase-like Hysteresis Loops in Electrodeposited Trisegmented Magnetic Nanowires: a Strategy toward Minimization of Interwire Interactions

Jin Zhang[†], Sebastià Agramunt-Puig[†], Núria Del-Valle[†], Carles Navau[†], Maria D. Baró[†], Sònia Estradé[‡], Francesca Peiró[‡], Salvador Pané[⊥], Bradley J. Nelson[⊥], Alvaro Sanchez[†], Josep Nogués[#§], Eva Pellicer[*†], and Jordi Sort[*†§]

† Departament de Física, Universitat Autònoma de Barcelona, Bellaterra, E-08193 Barcelona, Catalonia, Spain
‡ LENS, MIND-IN2UB, Departament d'Electrònica, Universitat de Barcelona, Martí i Franquès 1, E-08028 Barcelona, Spain
⊥ Institute of Robotics & Intelligent Systems (IRIS), ETH Zürich, CH-8092 Zurich, Switzerland
Catalan Institute of Nanoscience and Nanotechnology (ICN2), CSIC and The Barcelona Institute of Science and Technology, Campus UAB, Bellaterra, 08193 Barcelona, Spain
§ Institució Catalana de Recerca i Estudis Avançats (ICREA), Barcelona, Catalonia, Spain

Abstract

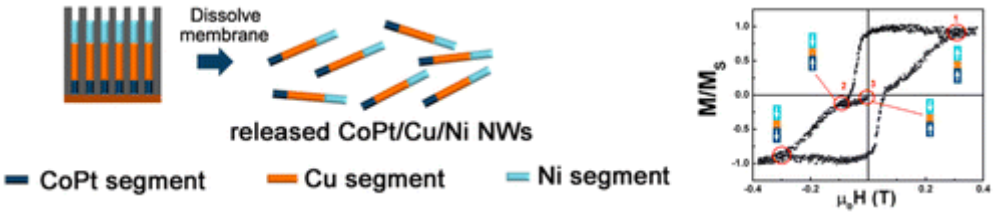

A new strategy to minimize magnetic interactions between nanowires (NWs) dispersed in a fluid is proposed. Such a strategy consists of preparing trisegmented NWs containing two antiparallel ferromagnetic segments with dissimilar coercivity separated by a nonmagnetic spacer. The trisegmented NWs exhibit a staircase-like hysteresis loop with tunable shape that depends on the relative length of the soft- and hard-magnetic segments and the respective values of saturation magnetization. Such NWs are prepared by electrodepositing CoPt/Cu/Ni in a polycarbonate (PC) membrane. The antiparallel alignment is set by applying suitable magnetic fields while the NWs are still embedded in the PC membrane. Analytic calculations are used to demonstrate that the interaction magnetic energy from fully compensated trisegmented NWs with antiparallel alignment is reduced compared to a single-component NW with the same length or the trisegmented NWs with the two ferromagnetic counterparts parallel to each other. The proposed approach is appealing for the use of

magnetic NWs in certain biological or catalytic applications where the aggregation of NWs is detrimental for optimized performance.

KEYWORDS:

- segmented nanowires
- magnetic interactions
- template-assisted electrodeposition
- staircase hysteresis loops
- nanomagnetism
-

1 Introduction

Owing to their unique physicochemical properties, materials structured in the form of one-dimensional nanoarchitectures, such as nanorods and nanowires (NWs), have found widespread applications in several technological areas, e.g., optoelectronics,(1) magnetism,(2, 3) catalysis,(4) piezo- and thermo-electricity,(5, 6) biosensing,(7, 8) and micro/nanoelectromechanical systems (MEMS/NEMS),(9) among others. Specifically, ferromagnetic NWs are being employed as components in information storage and logic devices,(3, 10, 11) spintronics,(12) magnetic sensors,(13) and also as platforms in the biomedical field (e.g., hyperthermia or drug delivery).(14)

For their range of applications to be expanded further, the implementation of other materials with dissimilar nature within the NW architecture can provide additional and complementary functionalities. The resulting hybrid structures (i.e., core–shell NWs or segmented NWs) offer enhanced performance due either to the established synergy between the properties of each building block or to interfacial interaction effects between them. Segmented NWs can be all electrodeposited in a cost-effective manner,(15-18) whereas core–shell NW structures usually require a combination of different synthetic approaches (e.g., electrodeposition together with chemical vapor deposition).(19) In the field of magnetism, segmented NWs served as a model system for heterostructured junctions that exhibit various fascinating perpendicular spin transport phenomena, such as current-perpendicular-to-plane giant magnetoresistance (GMR)(20, 21) or tunneling magnetoresistance (MR)(22) to name a couple. Likewise, core/shell NWs(23) combining several phases of distinct magnetic properties could generate additional effects, e.g., spintronic, multiferroic, magnetoplasmonic, and so forth. These outstanding properties have furnished hybrid NWs with a host of applications in giant magnetoresistance sensors,(24) spring-magnets,(25) exchange bias systems,(26) nanomagnet microwave resonators,(27) and magneto-plasmonic devices.(28)

Once released from the template or detached from the substrate, self-standing magnetic NWs can be dispersed in fluids and subsequently manipulated using external magnetic fields and field gradients. Wireless magnetic actuation is crucial for the utilization of these NWs in certain biological or catalytic applications.(18, 19, 29-31) However, one of the most challenging issues in areas like drug delivery or biological labeling is to avoid the aggregation of NWs once the external magnetic field is removed. Agglomeration of NWs inside bodily fluids can cause obstruction of the vessels, eventually leading to thrombosis or even more serious health diseases.

The formation of NW bundles is also a serious concern in applications that require the use of a single NW, for example, when a single NW is intended to be bound to cells or proteins(32) or in NWs that need to be precisely attached to small components to build sophisticated miniaturized devices.(33) Also, aggregation of NWs has to be prevented to obtain high-quality homogeneous ferrofluids or to preserve the mechanical properties of composites containing magnetic NWs.(13)

Magnetic dipolar interactions between magnetic particles dispersed in liquids are directly responsible for their agglomeration. In the absence of a magnetic field, such interactions are proportional to the overall remanent magnetization of each particle. For this reason, superparamagnetic nanoparticles, with zero net remanent magnetization, are usually preferred in comparison to NWs for certain biological applications.(31) Nevertheless, their exceedingly small surface area limits their efficiency as drug carriers. An alternative approach is to use magnetic vortices,(34) also with virtually zero magnetic remanence, but disks of a few micrometers in diameter are needed to form such magnetic configurations. Hence, magnetic vortices can be rather impractical for most biological purposes.

Ferromagnetic NWs offer some advantages with respect to superparamagnetic nanoparticles or microstructured disks exhibiting magnetic vortices. However, a smart strategy to tailor (and, in particular, to reduce) the overall remanent magnetization of magnetic NWs is needed to control (and decrease) the strength of interwire dipolar interactions to minimize aggregation. It is well-known that some of the properties of magnetic NWs (e.g., the effective magnetic anisotropy direction or the coercivity) are strongly dependent on the diameter and aspect ratio as well as on the dipolar coupling between the ferromagnetic segments.(35) For example, Liu and co-workers(36) have electrodeposited Co/Cu multilayered NWs in which the magnetic configurations can be tuned by adjusting the Co segment aspect ratio. In turn, the saturation magnetization depends mainly on the composition of the NWs.

In this work, the possibility to tune the remanent magnetization of NWs is demonstrated by synthesizing trisegmented NWs in which the orientation of the different segments comprising the NWs is individually controlled similarly to what has been successfully demonstrated in synthetic ferrimagnets,(37) patterned multilayers for multibit data storage,(38) or recently proposed in core/shell nanoparticles.(39, 40) To this end, arrays of trisegmented CoPt/Cu/Ni NWs (i.e., hard- and soft-ferromagnetic segments separated by a nonmagnetic Cu spacer) embedded in polycarbonate (PC) membranes have been prepared by electrodeposition. Magnetic measurements of the hybrid NWs, while still embedded in the PC templates, reveal the occurrence of staircase-like hysteresis loops resulting from the two different coercivities of the soft and hard ferromagnetic segments. The overall shape of the hysteresis loops (i.e., the magnetization step sizes) can be tuned by varying the aspect ratio of the different segments. Antiparallel alignment between the CoPt and Ni segments can be established after saturation by applying a negative magnetic field larger than the coercivity exhibited by Ni but lower than the coercivity corresponding to CoPt. In such antiparallel alignment, proper adjustment of the Ni and CoPt segment length leads to either positive or negative remanent magnetization, eventually even resulting in zero remanent net magnetization (fully compensated NWs). The trisegmented NWs can be easily released from the PC membrane and satisfactorily dispersed in fluids. Analytical calculations are used to corroborate that the interaction magnetic energy between two fully compensated trisegmented NWs (with two antiparallel magnetic segments) is

generally reduced with respect to a trisegmented NW having the two segments parallel to each other.

2 Experimental Section

2.1 Synthesis of the Trisegmented NWs

Template-assisted electrodeposition was carried out in a typical single-compartment double-jacketed glass electrochemical cell. Track-etched PC membranes with 30 nm nominal pore size (Nuclepore, Whatman) were used as working electrodes (WE). PC membranes with well-separated pores were selected for two reasons: (i) these membranes can afford the basic pH values needed to grow CoPt, and (ii) the distance between neighboring NWs is sufficiently high to ensure that interwire dipolar magnetic interactions between NWs are negligible such that their behavior when still embedded in the PC membrane is essentially the same as that of an isolated noninteracting NW. The fabrication process of trisegmented NWs is illustrated in Scheme 1.

Scheme 1

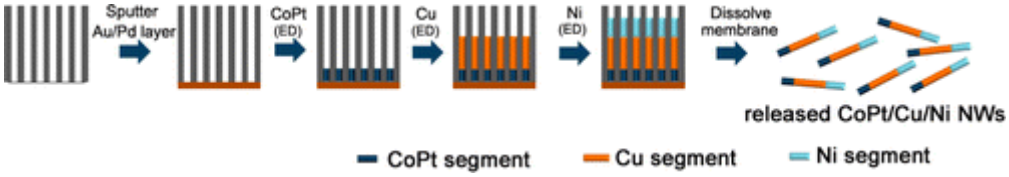

Scheme 1. Schematic Picture of the Trisegmented NW Fabrication Process Using PC Template-Based Electrodeposition (ED)

First, a thin Au–Pd layer was sputtered onto one side of PCs to make them conductive. The Au–Pd surface was put in contact with a copper plate and held inside a plastic stationary holder, and a circular area of 3.14 cm^2 was exposed to the electrolyte for deposition. Before electrodeposition, the PC membrane was placed in an ultrasonicator for 3 min to remove the air inside the PC channels. In this way, the electroactive species can penetrate inside the channels and access the Au–Pd layer, thereby enabling the electrodeposition. A platinum wire was utilized as counter electrode, which was positioned vertically facing the WE. A double junction Ag|AgCl 3 M KCl electrode (E = +0.210 V versus standard hydrogen electrode) was used as the reference electrode to record the potential at the WE. The three electrodes were connected to a PGSTAT302N Autolab potentiostat/galvanostat (Ecochemie).

The trisegmented NWs were prepared via sequential direct current electrodeposition of CoPt, Cu, and Ni segments by changing the corresponding electrolytes. The deposition of the CoPt segments was performed galvanostatically at j = −10 mA cm^{-2}, pH 8.5, and T = 65 °C. The electrolyte consisted of 30 mM $Co(SO_3NH_2)_2 \cdot xH_2O$, 2 mM $Pt(NH_3)_2(NO_2)_2$, 0.1 M glycine, 0.1 M sulfamic acid, 5 mM saccharine, and 0.1 M sodium citrate. The electrodeposition of Cu segments was carried out potentiostatically at E = −1.0 V in an electrolyte containing 0.2 M $CuSO_4 \cdot 5H_2O$ and 0.1 M boric acid. The third segment (Ni) was grown galvanostatically at j = −10 mA cm^{-2} from an electrolyte consisting of 2 M NH_4Cl and 0.1 M $NiCl_2$. The deposition processes for Cu and Ni segments were carried out at 25 °C, and the pH was left unadjusted (i.e., preparation pH). All of the electrolytes were deaerated before and during the experiments to get rid

of dissolved oxygen and to ensure the homogeneity of the solution. For electron microscopy observations, the trisegmented NWs were released by dissolving the PC template in chloroform and washed several times afterwards. For the sake of comparison, single-component Ni, Cu, and CoPt NWs were also electrodeposited using the same conditions as for the hybrid NWs.

2.2 Structural Characterization

Scanning electron microscopy (SEM) images and energy-dispersive X-ray spectroscopy (EDX) compositional analyses were acquired using a Merlin Zeiss microscope operated at 3 and 15 kV, respectively. Specimens for SEM and EDX measurements were prepared via drop-casting a droplet of NWs suspended in chloroform onto aluminum foil and subsequently dried in air. A similar preparation method onto Cu grids was used for TEM observations. The structure and morphology of the NWs (length of the different segments, aspect ratio, etc.) were also investigated by high-resolution transmission electron microscopy (HRTEM) using a Jeol-JEM 2011 system with a field emission gun operating at 200 kV. Electron energy loss spectra (EELS) were acquired along the NWs. Spectra were taken in the 650–1150 eV energy loss range, where the Co L2,3, Cu L2,3, and Ni L2,3 edges were found at 779, 931, and 855 eV, respectively. The quantitative analysis of the EELS spectra was performed using the homemade software package Oxide Wizard.(41) X-ray diffraction (XRD) patterns of the NWs were recorded on a Philips X'Pert diffractometer in the 30–100° 2θ range (step size = 0.026°, step time = 2000 s) using Cu Kα radiation (λ = 0.154178 nm). In this case, the PC membrane was not dissolved, and the XRD patterns were acquired while the NWs were still embedded inside the membrane.

2.3 Magnetic Characterization

Hysteresis loops were collected on the single-component (CoPt and Ni) and trisegmented (CoPt/Cu/Ni) NWs at room temperature using a vibrating sample magnetometer (VSM) from Oxford Instruments with a maximum applied magnetic field of 0.5 T. An antiparallel alignment between the CoPt and Ni segments was settled by first saturating the NWs in the positive direction and then applying a negative magnetic field sufficient to reverse Ni but lower than the coercivity of the CoPt segment.

3 Results and Discussion

3.1 Structure and Magnetic Behavior of Single-Component CoPt and Ni

All of the investigated NWs were deposited inside the channels (i.e., pores) of PC membranes that are visible as black spots by SEM imaging (see Figure S1 in the Supporting Information). These pores traverse the membranes completely, hence allowing the growth of the NWs by electrodeposition. The thickness of the PC membranes is approximately 5 μm, the average pore diameter (at the surface of the PC template) ranges from 40 to 60 nm, and there is an areal density of less than 10 pores μm^{-2}. Single-component NWs consisting of CoPt alloy, Cu, and Ni were first deposited individually to estimate and optimize the growth rates.

Figure 1

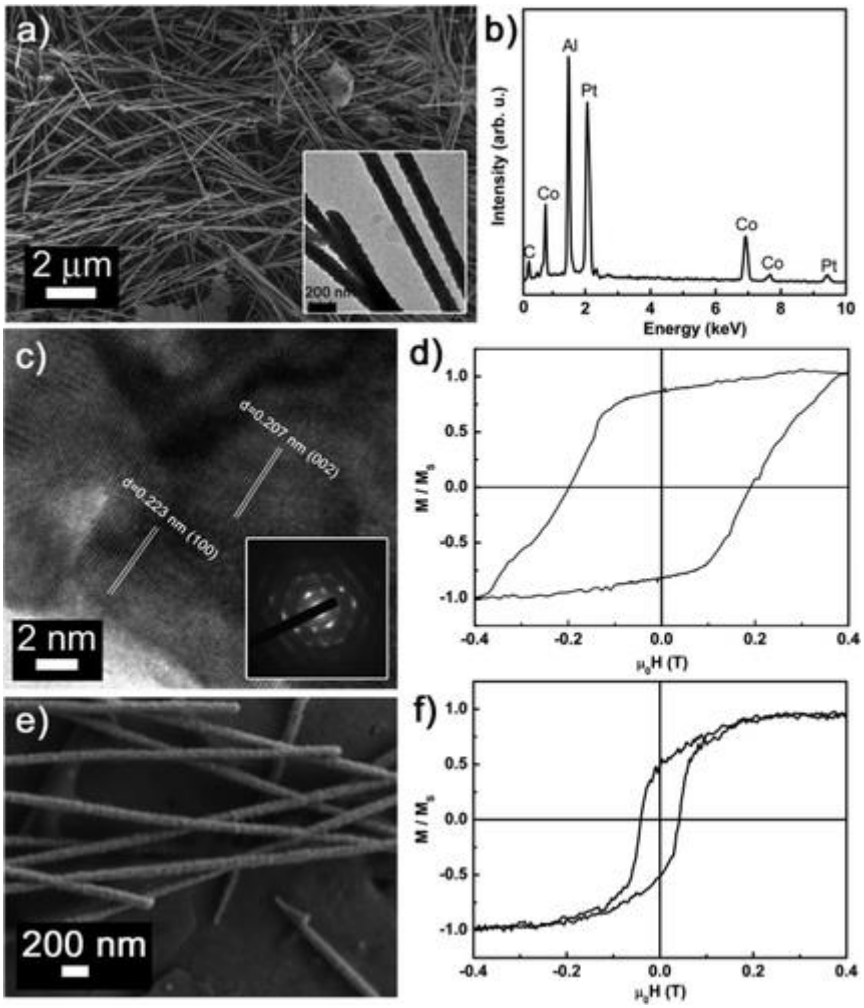

Figure 1. (a) SEM, (b) EDX spectrum, and (c) HRTEM image of CoPt NWs released from the PC membrane; (d) room-temperature magnetic hysteresis loop of single-component CoPt NWs arrays (measured before PC removal, along the NWs axis); (e) SEM image of single-component Ni NWs released from the PC membrane, and (f) room temperature hysteresis loop of single-component Ni NWs arrays (embedded in the PC membrane). Inset in (a) shows a magnified view of a few CoPt NWs, whereas the inset in (c) shows an SAED pattern of CoPt NWs.

As shown in Figure 1a, CoPt NWs can be obtained in high-yields with a length of around 5 µm and a diameter of approximately 100 nm (see also the corresponding TEM image, inset of Figure 1a). The larger diameter of the NWs, as compared to the average pore diameter at the surface of the PC membranes, indicates that the channels inside the PC are probably not completely homogeneous in width. This is actually supported by previous works in the literature in which it has been suggested that the pores inside PC templates are not completely cylindrical (with a constant cross-section) but instead appear to be “cigar-like shaped”.(42) The NWs have all similar lengths, suggesting that their growth proceeds at the same rate over the whole PC area. This is an important feature for the subsequent fabrication of the trisegmented NWs. The EDX spectrum (Figure 1b) confirms that the NWs are composed of Pt and

Co with a mean atomic composition of $Co_{70}Pt_{30}$. The aluminum signal in Figure 1b comes from the aluminum foil onto which the NWs were drop-casted. The HRTEM and the associated SAED pattern (Figure 1c and inset) reveal that the CoPt NWs are polycrystalline (hexagonal closed-packed, hcp, phase) with clear lattice fringes. The obtained interplanar distances can be ascribed to the (100) and (002) planes of hcp structure. Representative SEM images of the Ni and Cu single-component NWs are shown in Figure 1e and Figure S2, respectively. Similar to CoPt NWs, well-grown continuous Cu and Ni NWs can be deposited with an approximate diameter of 100 nm.

Typical XRD patterns of the as-deposited CoPt, Cu, and Ni NWs embedded in the PC membrane are shown in Figure 2. For both Cu and Ni single-component NWs, the (111), (200), (220), and (311) reflections of the face-centered cubic (fcc) structure are detected. In addition, for Cu NWs, by comparing the tabulated and experimental relative peak intensities (*I*) of the (111) and (200) reflections, clear conclusions regarding the crystallographic texture can be drawn.

Figure 2

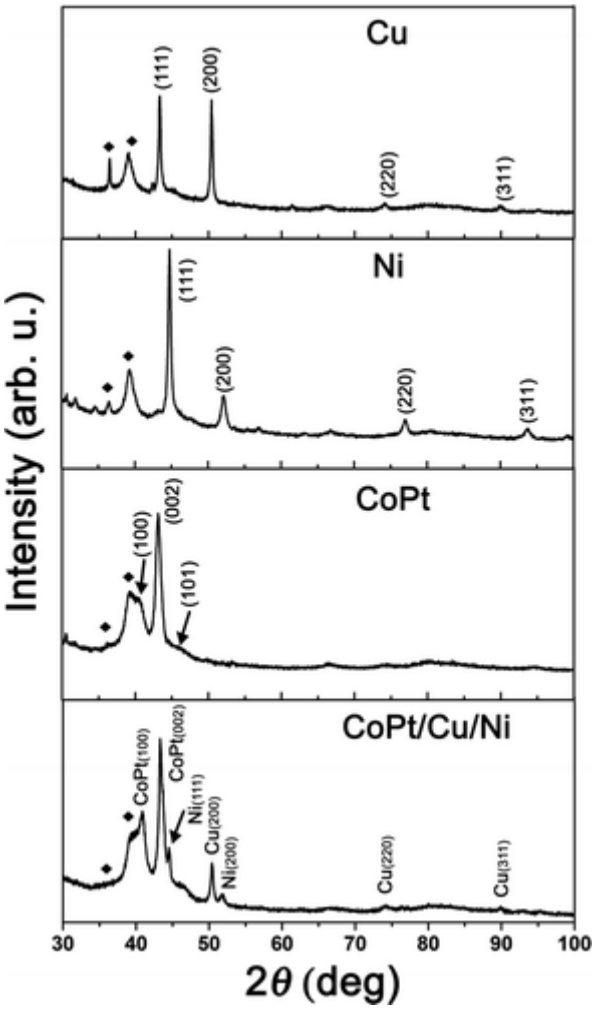

Figure 2. XRD patterns of single-component Cu, Ni, and CoPt NWs and trisegmented CoPt/Cu/Ni NWs. Peaks denoted by ♦ belong to the sputtered Au–Pd conductive layer.

Namely, the experimental I_{200}/I_{111} ratio is 1.02, which is larger than the theoretical value (0.46) for randomly oriented Cu grains. This indicates the formation of [100] textured Cu NWs. Textures in electrodeposited materials are highly influenced by electrolyte composition and working conditions. Thus, either nontextured or textured materials can be readily obtained by simply changing the plating parameters.

The diffractogram of single-component CoPt NWs reveals that the strongest peak appears at 2θ = 43.13°. This position matches both hcp and fcc phases. However, the absence of any reflection at ∼51.5° suggests that CoPt has crystallized in the hcp structure, as it corresponds to Co-rich NWs electrodeposited in basic pH conditions.(43) The intensity of the (101) reflection is dramatically reduced as compared to the standard powder pattern, which suggests that the hexagonal *c* axis lies preferentially along the long axis of the NWs.

The magnetic hysteresis loop of the single-component CoPt NW arrays measured with the applied field parallel ($H_{//}$) to the long axis of the NWs is shown in Figure 1d. The coercivity, H_C, is ∼1950 Oe. Therefore, CoPt NWs show hard ferromagnetic behavior. The magnetic properties of single-component Ni NWs were measured under the same conditions as for CoPt NWs. As shown in Figure 1f, H_C is around 410 Oe in this case. According to these data, it is clear that hard magnetic/spacer/soft magnetic trisegmented CoPt/Cu/Ni NWs could be, in principle, successfully deposited into PC membranes by simply changing the electrolyte.

3.2 Structural Characterization of Trisegmented NWs

The XRD pattern of the as-deposited trisegmented CoPt/Cu/Ni NW arrays embedded in the PC membrane is shown at the bottom of Figure 2. By comparing the XRD patterns of single-component and trisegmented CoPt/Cu/Ni NWs, all of the peaks corresponding to CoPt, Cu, and Ni phases can be straightforwardly indexed. Hence, the sequential fabrication process did not introduce any extra phases or impurities. Therefore, CoPt/Cu/Ni trisegmented NWs can be successfully synthesized through a template-based electrodeposition method.

Figure 3

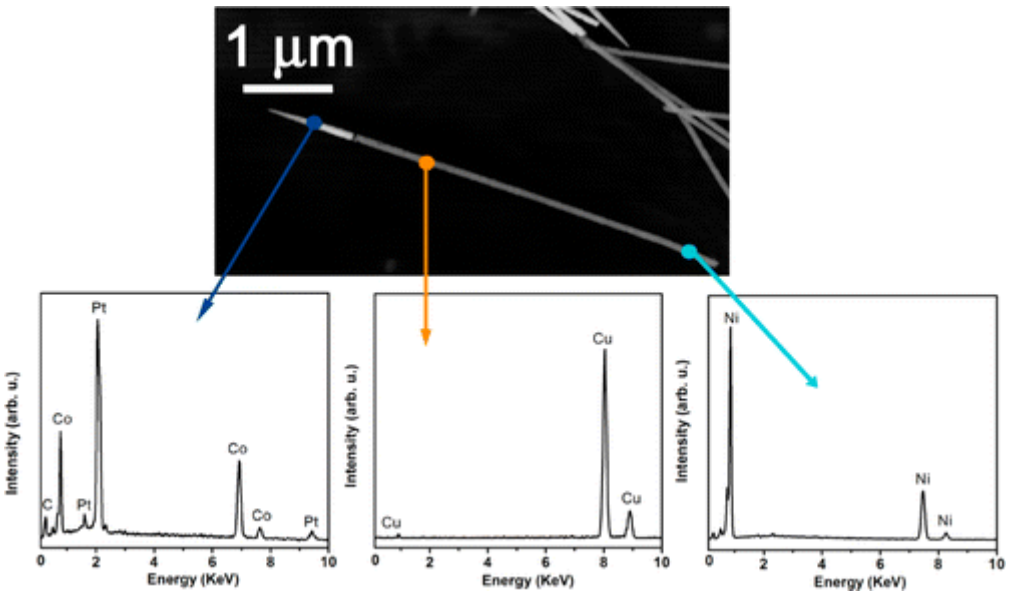

Figure 3. EDX spectra acquired in each of the segments of the trisegmented NW shown in the upper TEM image. Note that no clear interface between Cu and Ni can be seen using standard TEM conditions.

The compositional variations along the NW axis were assessed by EDX (see Figure 3). A TEM image of a whole trisegmented NW can be observed in the upper panel of Figure 3. NWs show a sharp needle-like end due to the narrowing of the PC pores near the surface, in agreement with the literature.(42) The darker and brighter contrast reveals the difference in atomic weight between the constituent phases with the electron dispersing capability of CoPt being stronger than for both Cu and Ni. Because Cu and Ni have similar atomic weights, it is difficult to clearly distinguish them by TEM. Therefore, the brightest region stands for CoPt and the darker regions represent the Cu + Ni segments.

Figure 4

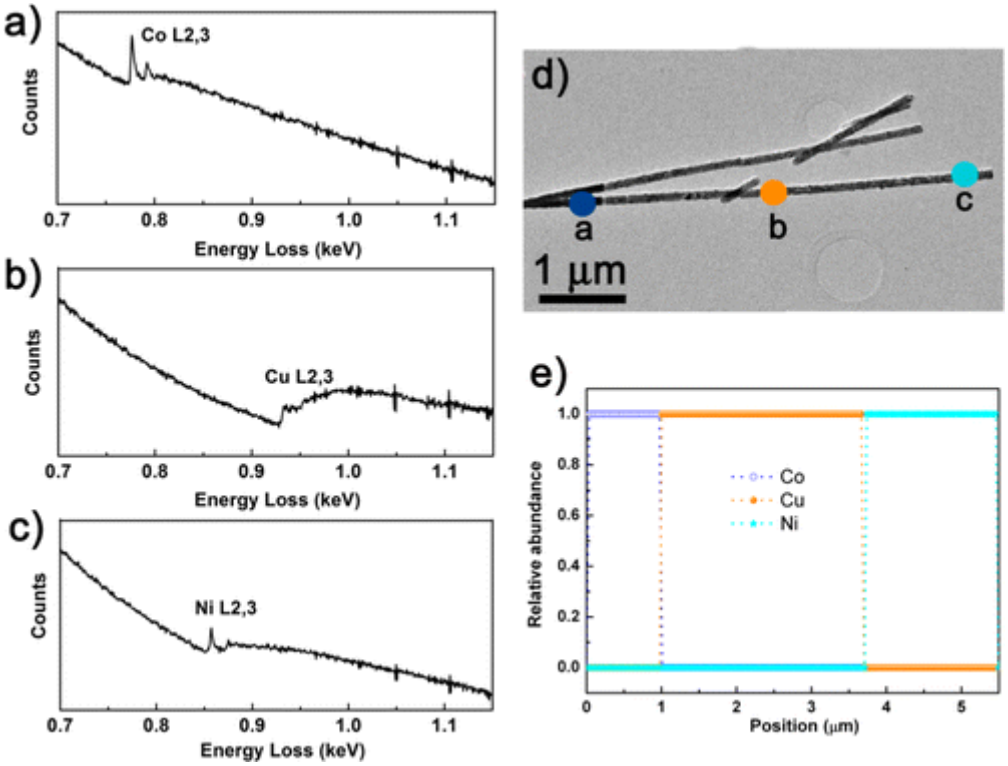

Figure 4. (a–c) EELS point spectra for CoPt/Cu/Ni trisegmented NWs [marked as a, b and c in (d)]. (d) STEM image of a CoPt/Cu/Ni trisegmented NW for which an EELS line-scan was performed. (e) The corresponding element distribution as a function of NW length.

For gaining further insight into the heterostructured architecture of the NWs, STEM-EELS analyses were performed (Figure 4). EELS analyses were actually necessary to distinguish between the Cu and Ni segments and, in turn, to determine their lengths. When the electron beam was spotting in “a”, Co was detected (Figure 4a). When the electron beam was directed to the middle part of the NW (point “b”), only Cu was visible (Figure 4b). Similarly, the EELS analysis on point “c” (Figure 4c) clearly confirms that the ending segment of the NW is made of pure Ni. EELS line-scan was used to determine the length of the different segments, as shown in Figure 4d and e. In this particular case (referred to as “sample D” in section 3.3), the length of the CoPt

segment, which now corresponds to the darker region, is 0.97 μm, whereas the Ni segment has a length of 1.74 μm. Finally, the Cu segment, with a length of 2.72 μm, is sandwiched between CoPt and Ni. In turn, EELS analysis performed in the NWs with shorter Ni segments (sample A in section 3.3) reveals that the CoPt, Cu, and Ni segment lengths are 1.10, 2.63, and 0.61 μm, respectively.

3.3 Magnetic Characterization of the Trisegmented NWs

Hysteresis loops from various arrays of CoPt/Cu/Ni trisegmented NWs embedded in the PC membrane, measured along the NWs axis, are shown in Figure 5. The loops exhibit a staircase-like shape with two well-differentiated coercivities corresponding to the magnetization reversal of Ni (soft segment) and CoPt (hard segment), respectively. These two switching events can be clearly seen because (i) the magnetic dipolar interactions between neighboring NWs in the PC membranes are small (due to the large interpore distance) and (ii) the segments in each nanowire are separated by the nonmagnetic Cu spacer to avoid magnetic exchange interactions between CoPt and Ni. Otherwise, if the NWs were deposited close to each other (as in conventional anodized aluminum oxide templates), the loops would become tilted, and the staircase shape would be lost.(44) Similarly, in the absence of the Cu segments, the interfacial coupling between Ni and CoPt would promote a simultaneous switching of the magnetization in both magnetic segments. Hence, this configuration of the trisegmented NWs provides access to various magnetization states depending on the relative orientation of the magnetization in each segment, as indicated in Figure 5b.

Figure 5

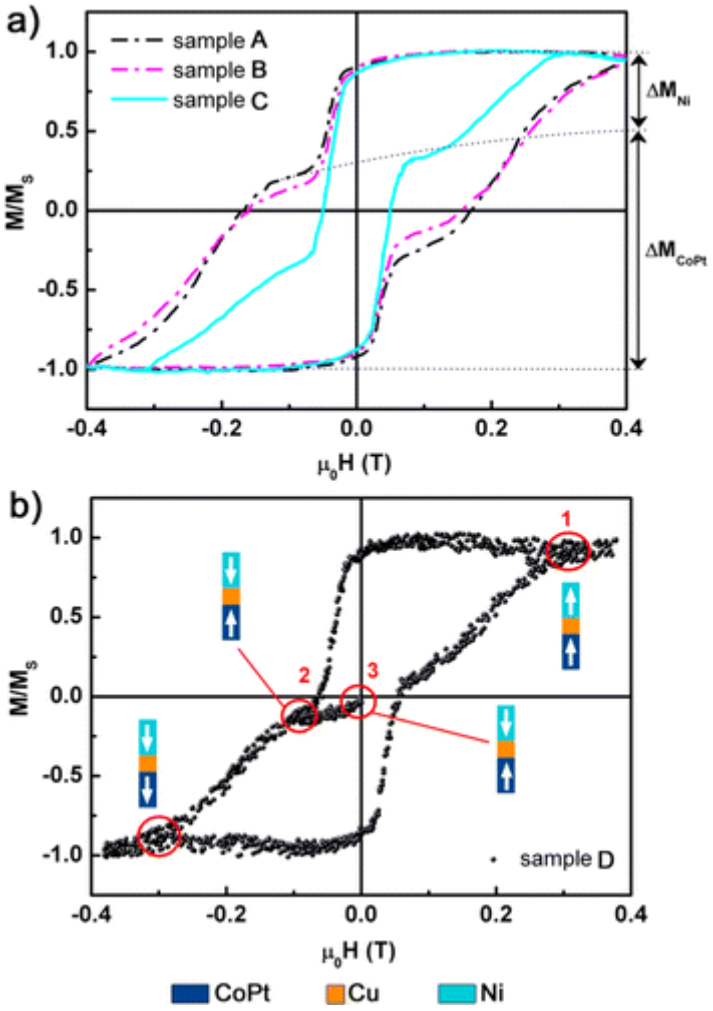

Figure 5. (a) Staircase-shaped hysteresis loops corresponding to trisegmented CoPt/Cu/Ni NWs with variable relative length ratios of the soft (Ni) and hard (CoPt) segments (samples A, B and C; see Table 1). (b) Hysteresis loop corresponding to an array of trisegmented CoPt/Cu/Ni NWs (sample D), where the magnetization amplitudes of the Ni (ΔM_{Ni}) and CoPt (ΔM_{CoPt}) segments are virtually equal to each other. Indications in (b) are the magnetic orientations of the two segments at different positions of the hysteresis loop.

Figure 5a reveals that although the contribution of Ni to the overall magnetization is larger than that of CoPt in sample C (in which the Ni segment is much longer than CoPt), the opposite is observed in samples A and B. Remarkably, the hysteresis loop shown in Figure 5b (sample D) exhibits virtually equal magnetization amplitudes from Ni and CoPt. Such precise tailoring of the hysteresis loop shape can be accomplished by varying the relative lengths of the Ni and CoPt segments (see Table 1). Because the saturation magnetization of Ni ($\mu_0 M_{S,Ni}$ = 0.6 T)(45) is approximately half that of CoPt ($\mu_0 M_{S,CoPt} \approx$ 1–1.3 T),(46, 47) the compensated situation (Figure 5b) occurs when the length of the Ni segment is approximately twice the length of CoPt (Table 1). In other words, in sample D (which is the one that corresponds to the EELS results shown in Figure 4) one has $\mu_0 M_{S,Ni} \times l_{Ni} \times A \approx \mu_0 M_{S,CoPt} \times l_{CoPt} \times A$ (where, l designates "length" and A is the cross-sectional area of the segments).

Table 1. Dependence of the Relative Magnetization Amplitudes of the CoPt (ΔM_{CoPt}) and Ni (ΔM_{Ni}) segments as Well as the Resulting Remanent Magnetization Once the Two Segments are Oriented Antiparallel to Each Other As Depicted in Figure 5b as a Function of the Average Relative Lengths of the CoPt (l_{CoPt}) and Ni (l_{Ni}) segments[a]

Sample	$< l_{CoPt} > / < l_{Ni} >$	$\Delta M_{CoPt}/\Delta M_{Ni}$	$M_{r,minor}/M_S$
A	~ 1.8	~ 3.2	0.31
B	~ 1.1	~ 2.2	0.23
C	~ 0.3	~ 0.6	–0.20
D	~ 0.5	~ 1.0	0

[a]

Note that $M_{r,minor}$ is not the overall remanence magnetization of the whole hysteresis loop (which is close to 1 in all cases) but instead denotes the remanent magnetization obtained when performing the minor loop sequence to set the antiparallel alignment between Ni and CoPt segments (i.e., when sweeping the field from positions 1 → 2 → 3 as indicated in Figure 5b. Samples A–D correspond to the ones whose hysteresis loops are shown in Figure 5.

3.4 Strategy to Minimize Interwire Interactions

As mentioned in the Introduction, magnetic NWs are appealing for various technological applications (biomedical, catalytic, MEMS/NEMS, etc.), but the strength of interwire magnetic interactions, once the NWs are dispersed in a fluid, needs to be controlled and minimized to attain optimized performance. By taking advantage of the staircase shape of the hysteresis loops, it is possible to engineer a protocol to set an antiparallel alignment between the soft and hard segments and therefore reduce the overall remanent magnetization of the NWs when they are still embedded in the PC template. This can be done by first saturating the array of NWs using a strong positive magnetic field (position 1 in Figure 5b) and then applying a negative field sufficient to switch Ni to the negative orientation without reversing the magnetization of CoPt (position 2). Once the magnetic field is brought back to zero (position 3), the two segments remain antiparallel to each other, and the resulting remanent magnetization ($M_{r,minor}$) will depend on the relative magnetization amplitudes of the Ni and CoPt segments (ΔM_{Ni} and ΔM_{CoPt}), i.e., on their length. The procedure is indicated in Figure 5b. Then, $M_{r,minor}/M_S$ can have either a positive value (samples A and B), negative value (sample C), or be virtually zero (sample D) (see Table 1). A comparative analytic calculation to show how the magnetic interaction energy outside the trisegmented NW in sample D is reduced when the two segments are antiparallel to each other, with respect to the case of parallel alignment, is given in section 3.5. It is worth mentioning that such antiparallel alignment between the soft and hard segments will remain in the

NWs dispersed in the fluid provided that the applied external magnetic fields used to manipulate them do not exceed the coercivity of the soft segment. Fortunately, wireless manipulation of magnetic NWs in low Reynolds number aqueous environments is actually possible under the action of external fields of only a few tens of Oe if combined with suitable magnetic field gradients.(48)

Figure 6

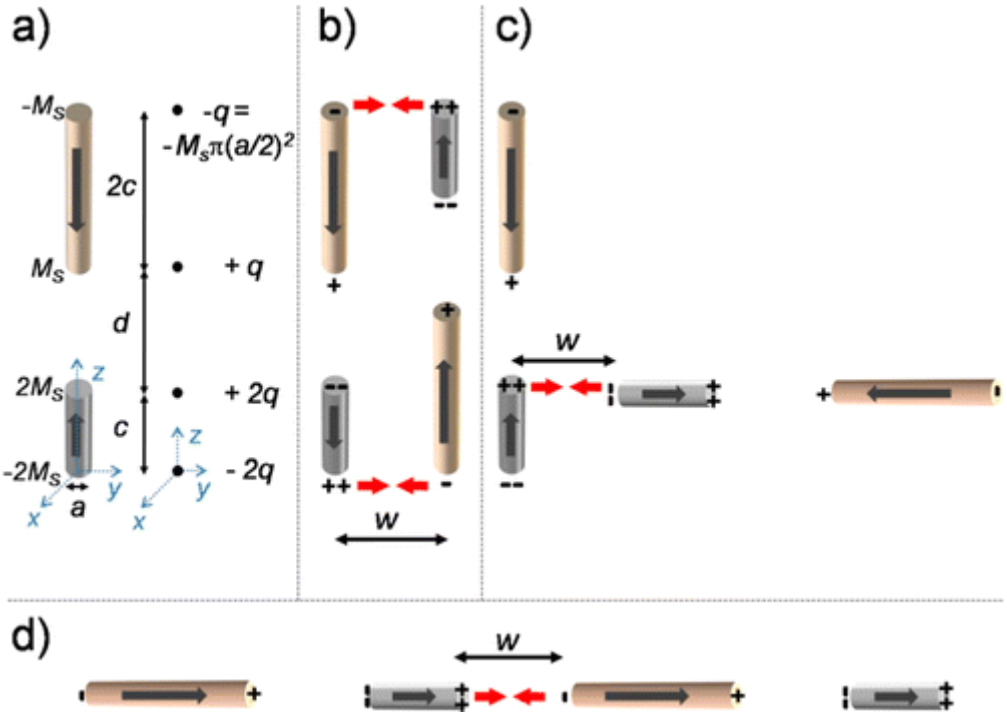

Figure 6. (a) (left) Schematic portrayal of a trisegmented NW in antiferromagnetic (compensated) arrangement, where the hard segment (bottom) has length *c* and saturation magnetization 2 M_S, and the soft segment (top) has length *c* and saturation magnetization M_S. The nonmagnetic segment is represented by the empty space of length *d* between the magnetic segments. The NW has diameter *a*. (right) Simplified representation of the NW as a set of point magnetic charges. (b–d) Different arrangements of NWs with attractive interactions (possibly leading to agglomeration) depending on the magnetization alignment between the magnetic segments, where *w* is the distance between wires. The symbols + and – indicate the sign of the equivalent charges, and the red arrows represent an attractive interaction between NWs.

3.5 Modeling the Magnetic Interaction Energy between Two Trisegmented NWs

For the sake of simplicity, we assume that each fully compensated trisegmented NW has a circular cross-section of diameter *a* and that it is composed of a hard segment of length *c* and uniform magnetization $2M_S$, a soft segment of length 2*c* and uniform magnetization M_S, and a nonmagnetic segment represented by an empty space of length *d* between the two magnetic segments (left of Figure 6a). To some extent, this theoretical NW can be approximated as a set of pairs of point magnetic charges. That is, the hard segment is assumed equivalent to two charges of values −2*q* and 2*q*,

where q corresponds to $M_S\pi a^2/4$, located at the center of the lower and upper surfaces of the segment, respectively. In the same way, the soft segment can be simplified as two charges of values q and $-q$ located at the center of the lower and upper surfaces, respectively (right of Figure 6a). The sign of each pair of charges changes depending on the orientation of the segment magnetization. For simulating the NWs of sample D, the dimensions of the NWs are $a = c/10$ and $d = 2.5c$.

Once the NWs are properly magnetized (with the two segments aligned parallel or antiparallel) and dispersed in the fluid, they can be oriented in any direction. The relative orientation between two NWs can cause some attractive or repulsive movements between them because of the magnetic interaction that can result in the agglomeration of NWs. Figure 6 shows the possible ways of attractive interaction between NWs with antiparallel magnetic segments (Figure 6c) or parallel magnetic segments (Figures 6b and d). The symbols + , ++, – and – – represent the equivalent charges $+q$, $+2q$, $-q$, and $-2q$, respectively, in the point charge approximation. In the case of antiparallel segments, the NWs would be mainly attracted by forming a T-shape (Figure 6c), and in the parallel case, the NWs would be attracted by following an antiferromagnetic coupling (Figure 6b) or by aligning one along the other (Figure 6d). Other configurations of NW interactions have weaker attractive interactions.

To analyze which NW configurations have lower magnetic attraction and thus a weaker possibility of agglomeration, we plot in Figure 7 a comparison of the energies of the three different arrangements sketched in Figure 6. The magnetic interaction energy (normalized to $\mu_0 q^2/c$) of two NWs is plotted as a function of their distance w (normalized to c) when $d = 2.5c$. The results reveal that, for interwire distances $w < c$, the interaction between T-shape NWs with antiparallel segments (solid black line) is lower than the one obtained in the case of antiferromagnetically coupled NWs with parallel segments (dashed red line). In these results, the size of the nonmagnetic segment is a relevant parameter because if $d < c$ the “T-shape” NW configuration becomes the one with the largest interaction (not shown). Note that for interwire distances $w < 0.1c$ (that is $w < a$), the model of point charges is no longer valid. The inset of Figure 7 shows the case of large interwire distances with the same interaction energies plotted in logarithmic scale (in absolute value). For comparison, the dependences $1/w^3$ (thin solid green line) that correspond to a dipole–dipole magnetic interaction and $1/w^5$ (thin dashed orange line) that correspond to a quadrupole–quadrupole magnetic interaction are also plotted. These calculations reveal that for large interwire distances ($w > 50c$) the interaction between T-shape NWs is the lowest and decays as $1/w^5$ (black line is parallel to the orange one), whereas for the configurations with parallel segment NWs, it decays as $1/w^3$ (red and blue lines are parallel to the green one).

The results of this section demonstrate theoretically that the agglomeration power between NWs with parallel magnetic segments is always larger than for NWs with antiparallel segments. The results do not qualitatively change when considering charged surfaces instead of point charges.

Figure 7

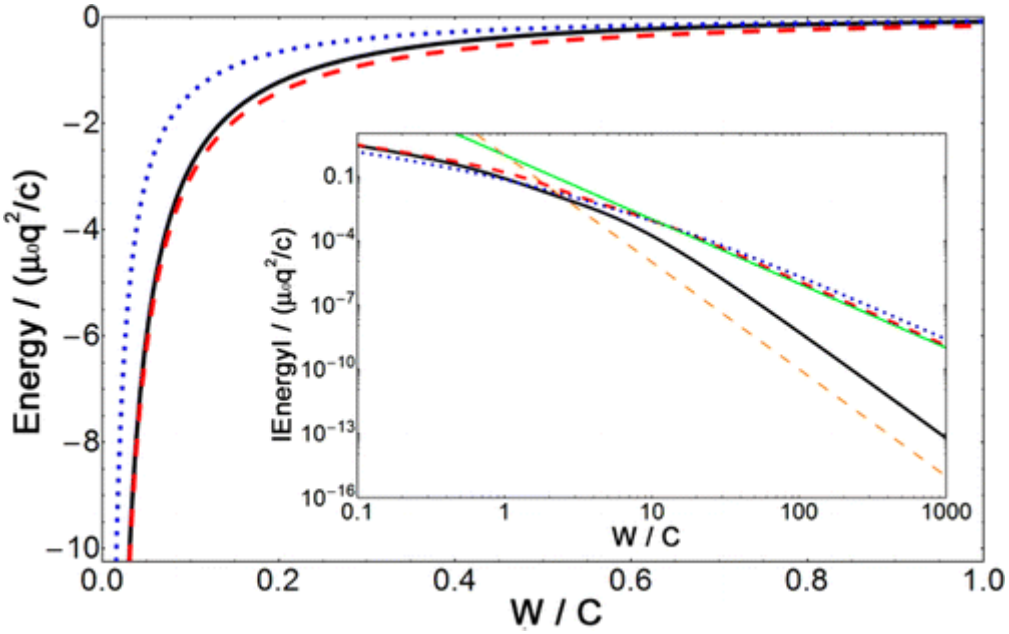

Figure 7. Interaction energy as a function of separation *w* between the NWs when *d* = 2.5*c* for the different NW configurations of Figure 6: parallel magnetization alignment of Figure 6b (dashed red line), antiparallel alignment of Figure 6c (solid black line), and parallel alignment of Figure 6d (dotted blue line). The inset shows the absolute value of the energy of the main plot on a logarithmic scale. For comparison, the dependences $1/w^3$ (thin solid green line) and $1/w^5$ (thin dashed orange line) are also plotted in the inset.

4 Conclusions

In summary, arrays of trisegmented CoPt/Cu/Ni NWs with tunable segment lengths have been satisfactorily electrodeposited inside the pores of PC membranes and subsequently further characterized both structurally and magnetically. These NWs exhibit staircase-like hysteresis loops resulting from the two different coercivities of the soft (Ni) and hard ferromagnetic (CoPt) segments. The magnetization amplitudes of the two ferromagnetic contributions depend on the relative lengths of CoPt and Ni. Antiparallel alignment between both ferromagnetic segments can be settled after positive saturation by applying a negative magnetic field sufficient to switch the Ni magnetization but smaller than the CoPt coercivity. In such antiparallel alignment, proper adjustment of the Ni and CoPt segment lengths eventually leads to virtually zero remanent magnetization (fully compensated NWs). The trisegmented NWs can be then released from the PC membrane and satisfactorily dispersed in fluids. Analytical calculations are employed to corroborate that the magnetic interaction energy between two fully compensated trisegmented NWs (with two antiparallel magnetic segments with the same overall magnetic moment) is reduced with respect to a single NW with the same length or the trisegmented NW with the two segments parallel to each other. Hence, this strategy is suitable to decrease the strength of magnetic interactions between NWs dispersed in liquids and is thus very appealing in all applications

requiring the utilization of well-isolated magnetic single NWs as well as to minimize NW agglomeration during/after being used.

Acknowledgment

This work has been partially funded by the 2014-SGR-1015, 2014-SGR-150, and 2014-PROD-00059 projects from the Generalitat de Catalunya, the MAT2014-57960-C3-1-R (co-funded by FEDER), MAT2012-35370, MAT2013-41506 and CSD2009-00013 projects from the Spanish Ministerio de Economía y Competitividad (MINECO), and the MANAQA FET-Open Project from the European Commission (FP7) under Grant Agreement 296679 and the ERC CoG 648454 SPIN-PORICS. J.Z. is grateful to the China Scholarship Council (CSC) for a Ph.D. grant. E.P. is grateful to MINECO for the “Ramon y Cajal” contract (RYC-2012-10839). A.S. acknowledges a grant from ICREA Academia funded by the Generalitat de Catalunya. ICN2 acknowledges support from the Severo Ochoa Program (MINECO, Grant No. SEV-2013-0295).

References

1. **1**

   Brambilla, G. Optical Fibre Nanowires and Microwires: A Review J. Opt. **2010**, 12, 043001– 043020 DOI: 10.1088/2040-8978/12/4/043001

   [Crossref], [CAS], Google Scholar

2. **2**

   O’Brien, L.; Petit, D.; Lewis, E. R.; Cowburn, R. P.; Read, D. E.; Sampaio, J.; Zeng, H. T.; Jausovec, A.-V. Tunable Remote Pinning of Domain Walls in Magnetic Nanowires Phys. Rev. Lett. **2011**, 106, 087204 DOI: 10.1103/PhysRevLett.106.087204

   [Crossref], Google Scholar

3. **3**

Vázquez, M.; Vivas, L. G. Magnetization Reversal in Co-Base Nanowire Arrays Phys. Status Solidi B **2011**, 248, 2368– 2381 DOI: 10.1002/pssb.201147092

[Crossref], [CAS], Google Scholar

4. **4**

Sun, Y.; Zhang, F.; Xu, L.; Yin, Z.; Song, X. Roughness-Controlled Copper Nanowires and Cu nanowires–Ag Heterostructures: Synthesis and Their Enhanced Catalysis J. Mater. Chem. A **2014**, 2, 18583– 18592 DOI: 10.1039/C4TA03689A

[Crossref], [CAS], Google Scholar

5. **5**

Espinosa, H. D.; Bernal, R. A.; Minary-Jolandan, M. A Review of Mechanical and Electromechanical Properties of Piezoelectric Nanowires Adv. Mater. **2012**, 24, 4656– 4675 DOI: 10.1002/adma.201104810

[Crossref], [PubMed], [CAS], Google Scholar

6. **6**

Farhangfar, S. Size-Dependent Thermoelectricity in Nanowires J. Phys. D: Appl. Phys. **2011**, 44, 125403 DOI: 10.1088/0022-3727/44/12/125403

[Crossref], [CAS], Google Scholar

7. **7**

Yogeswaran, U.; Chen, S. A Review on the Electrochemical Sensors and Biosensors Composed of Nanowires as Sensing Material Sensors **2008**, 8, 290– 313 DOI: 10.3390/s8010290

[Crossref], [CAS], Google Scholar

8. **8**

Zheng, G.; Patolsky, F.; Cui, Y.; Wang, W. U.; Lieber, C. M. Multiplexed Electrical Detection of Cancer Markers with Nanowire Sensor Arrays Nat. Biotechnol. **2005**, 23, 1294– 1301 DOI: 10.1038/nbt1138

[Crossref], [PubMed], [CAS], Google Scholar

9. **9**

Fan, D. L.; Zhu, F. Q.; Cammarata, R. C.; Chien, C. L. Controllable High-Speed Rotation of Nanowires Phys. Rev. Lett. **2005**, 94, 247208 DOI: 10.1103/PhysRevLett.94.247208

[Crossref], Google Scholar

10. **10**

Kou, X.; Fan, X.; Dumas, R. K.; Lu, Q.; Zhang, Y.; Zhu, H.; Zhang, X.; Liu, K.; Xiao, J. Q. Memory Effect in Magnetic Nanowire Arrays Adv. Mater. **2011**, 23, 1393– 1397 DOI: 10.1002/adma.201003749

[Crossref], [PubMed], [CAS], Google Scholar

11. **11**

Parkin, S. S. P.; Hayashi, M.; Thomas, L. Magnetic Domain-Wall Racetrack Memory Science **2008**, 320, 190– 194 DOI: 10.1126/science.1145799

[Crossref], [PubMed], [CAS], Google Scholar

12. **12**

Zhang, Z.; Dai, Y.; Yu, L.; Guo, M.; Huang, B.; Whangbo, M.-H. The Surface Termination Effect on the Quantum Confinement and Electron Affinities of 3C-SiC Quantum Dots: A First-Principles Study Nanoscale **2012**, 4, 1592– 1597 DOI: 10.1039/c2nr12099b

[Crossref], Google Scholar

13. **13**

Winkler, A.; Mühl, T.; Menzel, S.; Kozhuharova-Koseva, R.; Hampel, S.; Leonhardt, A.; Büchner, B. Magnetic Force Microscopy Sensors Using Iron-Filled Carbon Nanotubes J. Appl. Phys. **2006**, 99, 104905 DOI: 10.1063/1.2195879

[Crossref], [CAS], Google Scholar

14. **14**

Choi, D. S.; Park, J.; Kim, S.; Gracias, D. H.; Cho, M. K.; Kim, Y. K.; Fung, A.; Lee, S. E.; Chen, Y.; Khanal, S.; Baral, S.; Kim, J.-H. Hyperthermia with Magnetic Nanowires for Inactivating Living Cells J. Nanosci. Nanotechnol. **2008**, 8, 2323– 2327 DOI: 10.1166/jnn.2008.273

[Crossref], Google Scholar

15. **15**

Prida, V. M.; García, J.; Iglesias, L.; Vega, V.; Görlitz, D.; Nielsch, K.; Barriga-Castro, E. D.; Mendoza-Reséndez, R.; Ponce, A.; Luna, C. Electroplating and Magnetostructural Characterization of Multisegmented $Co_{54}Ni_{46}/Co_{85}Ni_{15}$ Nanowires from Single Electrochemical Bath in Anodic Alumina Templates Nanoscale Res. Lett. **2013**, 8, 263 DOI: 10.1186/1556-276X-8-263

[Crossref], [PubMed], [CAS], Google Scholar

16. **16**

Choi, J.; Oh, S. J.; Ju, H.; Cheon, J. Massive Fabrication of Free-Standing One-Dimensional Co/Pt Nanostructures and Modulation of Ferromagnetism via a Programmable Barcode Layer Effect Nano Lett. **2005**, 5, 2179– 2183 DOI: 10.1021/nl051190k

[ACS Full Text], Google Scholar

17. **17**

Bangar, M. A.; Hangarter, C. M.; Yoo, B.; Rheem, Y.; Chen, W.; Mulchandani, A.; Myung, N. V. Magnetically Assembled Multisegmented Nanowires and Their Applications Electroanalysis **2009**, 21, 61– 67 DOI: 10.1002/elan.200804372

[Crossref], Google Scholar

18. **18**

Özkale, B.; Shamsudhin, N.; Chatzipirpiridis, G.; Hoop, M.; Gramm, F.; Chen, X.; Martí, X.; Sort, J.; Pellicer, E.; Pané, S. Multisegmented FeCo/Cu Nanowires: Electrosynthesis, Characterization, and Magnetic Control of Biomolecule Desorption ACS Appl. Mater. Interfaces **2015**, 7, 7389– 7396 DOI: 10.1021/acsami.5b01143

[ACS Full Text], [CAS], Google Scholar

19. **19**

Zeeshan, M. A.; Pané, S.; Youn, S. K.; Pellicer, E.; Schuerle, S.; Sort, J.; Fusco, S.; Lindo, A. M.; Park, H. G.; Nelson, B. J. Graphite Coating of Iron Nanowires for Nanorobotic Applications: Synthesis, Characterization and Magnetic Wireless Manipulation Adv. Funct. Mater. **2013**, 23, 823– 831 DOI: 10.1002/adfm.201202046

[Crossref], [CAS], Google Scholar

20. **20**

Piraux, L.; George, J. M.; Despres, J. F.; Leroy, C.; Ferain, E.; Legras, R.; Ounadjela, K.; Fert, A. Giant Magnetoresistance in Magnetic Multilayered Nanowires Appl. Phys. Lett. **1994**, 65, 2484– 2486 DOI: 10.1063/1.112672

[Crossref], Google Scholar

21. **21**

Liu, K.; Nagodawithana, K.; Searson, P. C.; Chien, C. L. Perpendicular Giant Magnetoresistance of Multilayered Co/Cu nanowires Phys. Rev. B: Condens. Matter Mater. Phys. **1995**, 51, 7381– 7384 DOI: 10.1103/PhysRevB.51.7381

[Crossref], Google Scholar

22. **22**

Doudin, B.; Redmond, G.; Gilbert, S. E.; Ansermet, J. – Ph. Magnetoresistance Governed by Fluctuations in Ultrasmall

Ni/NiO/Co Junction Phys. Rev. Lett. **1997**, 79, 933– 936 DOI: 10.1103/PhysRevLett.79.933

[Crossref], Google Scholar

23. **23**

Chong, Y. T.; Görlitz, D.; Martens, S.; Yau, M. Y. E.; Allende, S.; Bachmann, J.; Nielsch, K. Multilayered Core/Shell Nanowires Displaying Two Distince Magnetic Switching Events Adv. Mater. **2010**, 22, 2435– 2439 DOI: 10.1002/adma.200904321

[Crossref], Google Scholar

24. **24**

Piraux, L.; Renard, K.; Guillemet, R.; Mátéfi-Tempfli, S.; Mátéfi-Tempfli, M.; Antohe, V. A.; Fusil, S.; Bouzehouane, K.; Cros, V. Template-Grown NiFe/Cu/NiFe Nanowires for Spin Transfer Devices Nano Lett. **2007**, 7, 2563– 2567 DOI: 10.1021/nl070263s

[ACS Full Text], [CAS], Google Scholar

25. **25**

Gapin, A. I.; Ye, X. R.; Chen, L. H.; Hong, D.; Jin, S. Patterned Media Based on Soft/Hard Composite Nanowire Array of Ni/CoPt IEEE Trans. Magn. **2007**, 43, 2151– 2153 DOI: 10.1109/TMAG.2007.893121

[Crossref], [CAS], Google Scholar

26. **26**

Salabas, E. L.; Rumplecker, A.; Kleitz, F.; Radu, F.; Schuth, F. Exchange Anisotropy in Nanocasted Co_3O_4 Nanowires Nano Lett. **2006**, 6, 2977– 2981 DOI: 10.1021/nl060528n

[ACS Full Text], Google Scholar

27. **27**

Mourachkine, A.; Yazyev, O. V.; Ducati, C.; Ansermet, J. Template Nanowires for Spintronics Applications: Nanomagnet Microwave Resonators Functioning in Zero Applied Nano Lett. **2008**, 8, 3683– 3687 DOI: 10.1021/nl801820h

[ACS Full Text], Google Scholar

28. **28**

Zhang, Y.; Ashall, B.; Doyle, G.; Zerulla, D.; Lee, G. U. Highly Ordered Fe–Au Heterostructured Nanorod Arrays and Their Exceptional Near-Infrared Plasmonic Signature Langmuir **2012**, 28, 17101– 17107 DOI: 10.1021/la302290v

[ACS Full Text], Google Scholar

29. **29**

Su, Y.; Tang, J.; Yang, H.; Cheng, Z. Multifunctional Multisegmented Co/$CoPt_3$ Heterostructure Nanowires Nanoscale **2013**, 5, 9709– 9713 DOI: 10.1039/c3nr02767h

[Crossref], Google Scholar

30. **30**

Gao, W.; Manesh, K. M.; Hua, J.; Sattayasamitsathit, S.; Wang, J. Hybrid Nanomotor: A Catalytically/Magnetically Powered Adaptive Nanowire Swimmer Small **2011**, 7, 2047– 2051 DOI: 10.1002/smll.201100213

[Crossref], [PubMed], [CAS], Google Scholar

31. **31**

Alvarez-Lorenzo, C.; Concheiro, A. Smart Drug Delivery Systems: From Fundamentals to the Clinic Chem. Commun. **2014**, 50, 7743– 7765 DOI: 10.1039/c4cc01429d

[Crossref], [PubMed], [CAS], Google Scholar

32. **32**

Reich, D. H.; Tanase, M.; Hultgren, A.; Bauer, L. A.; Chen, C. S.; Meyer, G. J. Biological Applications of Multifunctional Magnetic Nanowires (invited) J. Appl. Phys. **2003**, 93, 7275– 7280 DOI: 10.1063/1.1558672

[Crossref], [CAS], Google Scholar

33. **33**

Gao, F.; Gu, Z. Nano-Soldering of Magnetically Aligned Three-Dimensional Nanowire Networks Nanotechnology **2010**, 21, 115604 DOI: 10.1088/0957-4484/21/11/115604

[Crossref], Google Scholar

34. **34**

Kim, D.-H.; Rozhkova, E. A.; Ulasov, I. V.; Bader, S. D.; Rajh, T.; Lesniak, M. S.; Novosad, V. Biofunctionalized Magnetic-Vortex Microdiscs for Targeted Cancer-Cell Destruction Nat. Mater. **2010**, 9, 165– 171 DOI: 10.1038/nmat2591

[Crossref], [PubMed], [CAS], Google Scholar

35. **35**

Chen, M.; Chien, C. L.; Searson, P. C. Potential Modulated Multilayer Deposition of Multisegment Cu/Ni Nanowires with Tunable Magnetic Properties Chem. Mater. **2006**, 18, 1595– 1601 DOI: 10.1021/cm052262b

[ACS Full Text], Google Scholar

36. **36**

Wong, J.; Greene, P.; Dumas, R. K.; Liu, K. Probing Magnetic Configurations in Co/Cu Multilayered Nanowires Appl. Phys. Lett. **2009**, 94, 032504 DOI: 10.1063/1.3073740

[Crossref], Google Scholar

37. **37**

Sort, J.; Rodmacq, B.; Auffret, S.; Dieny, B. Pinned Synthetic Ferrimagnets with Perpendicular Anisotropy and Tuneable Exchange Bias Appl. Phys. Lett. **2003**, 83, 1800– 1802 DOI: 10.1063/1.1606495

[Crossref], Google Scholar

38. **38**

Baltz, V.; Rodmacq, B.; Bollero, A.; Ferré, J.; Landis, S.; Dieny, B. Balancing Interlayer Dipolar Interactions in Multilevel Patterned Media with out-of-Plane Magnetic Anisotropy Appl. Phys. Lett. **2009**, 94, 052503 DOI: 10.1063/1.3078523

[Crossref], Google Scholar

39. **39**

Estrader, M.; López-Ortega, A.; Estradé, S.; Golosovsky, I. V.; Salazar-Alvarez, G.; Salazar-Alvarez, G.; Vasilakaki, M.; Trohidou, K. N.; Varela, M.; Stanley, D. C.; Sinko, M.; Pechan, M. J.; Keavney, D. J.; Peiró, F.; Surinach, S.; Baro, M. D.; Nogués, J. Robust Antiferromagnetic Coupling in Hard-Soft Bi-magnetic Core/Shell Nanoparticles Nat. Commun. **2013**, 4, 2960 DOI: 10.1038/ncomms3960

[Crossref], [PubMed], [CAS], Google Scholar

40. **40**

López-Ortega, A.; Estrader, M.; Salazar-Alvarez, G.; Roca, A. G.; Nogués, J. Applications of Exchange Coupled Bi-Magnetic Hard/soft and Soft/hard Magnetic Core/shell Nanoparticles Phys. Rep. **2015**, 553, 1– 32 DOI: 10.1016/j.physrep.2014.09.007

[Crossref], [CAS], Google Scholar

41. **41**

Yedra, L.; Xuriguera, E.; Estrader, M.; López-Ortega, A.; Baró, M. D.; Nogués, J.; Roldan, M.; Varela, M.; Estradé, S.; Peiró, F. Oxide Wizard: An EELS Application to Characterize the White Lines of Transition Metal Edges Microsc. Microanal. **2014**, 20, 698– 705 DOI: 10.1017/S1431927614000440

[Crossref], [PubMed], [CAS], Google Scholar

42. **42**

Schönenberger, C.; Van der Zande, B. M. I.; Fokkink, L. G. J.; Henny, M.; Schmid, C.; Krüger, M.; Bachtold, A.; Huber, R.; Birk, H.; Staufer, U. Template Synthesis of Nanowires in Porous Polycarbonate Membranes: Electrochemistry and Morphology J. Phys. Chem. B **1997**, 5647, 5497– 5505

Google Scholar

43. **43**

Jang, B.; Pellicer, E.; Guerrero, M.; Chen, X.; Choi, H.; Nelson, B. J.; Sort, J.; Pané, S. Fabrication of Segmented Au/Co/Au Nanowires: Insights in the Quality of Co/Au Junctions ACS Appl. Mater. Interfaces **2014**, 6, 14583– 14589 DOI: 10.1021/am5038998

[ACS Full Text], [CAS], Google Scholar

44. **44**

Agramunt-Puig, S.; Del-Valle, N.; Pellicer, E.; Zhang, J.; Nogués, J.; Navau, C.; Sanchez, A.; Sort, J. Modeling the Collective Magnetic Behavior of Highly-packed Arrays of Multi-segmented Nanowires New J. Phys. **2016**, 18, 013026 DOI: 10.1088/1367-2630/18/1/013026

[Crossref], Google Scholar

45. **45**

Ferré, R.; Ounadjela, K.; George, J. M.; Piraux, L.; Dubois, S. Magnetization Processes in Nickel and Cobalt Electrodeposited Nanowires Phys. Rev. B: Condens. Matter Mater. Phys. **1997**, 56, 14066– 14075 DOI: 10.1103/PhysRevB.56.14066

[Crossref], [CAS], Google Scholar

46. **46**

Mitsuzuka, K.; Shimatsu, T.; Kikuchi, N.; Okamoto, S.; Aoi, H.; Kitakami, O. Remanence Coercivity of Dot Arrays of Hcp-CoPt Perpendicular Films J. Phys. Conf. Ser. **2010**, 200, 102005 DOI: 10.1088/1742-6596/200/10/102005

[Crossref], Google Scholar

47. **47**

Mallet, J.; Yu-Zhang, K.; Chien, C.-L.; Eagleton, T. S.; Searson, P. C. Fabrication and Magnetic Properties of Fcc Co_xPt_{1-x} Nanowires Appl. Phys. Lett. **2004**, 84, 3900– 3902 DOI: 10.1063/1.1739274

[Crossref], Google Scholar

48. **48**

Zhang, L.; Petit, T.; Lu, Y.; Kratochvil, B. E.; Peyer, K. E.; Pei, R.; Lou, J.; Nelson, B. J. Controlled Propulsion and Cargo Transport of Rotating Nickel Nanowires near a Patterned Solid Surface ACS Nano **2010**, 4, 6228– 6234 DOI: 10.1021/nn101861n

[ACS Full Text], [CAS], Google Scholar